Geometry of the Inkjet-Printed Sensing Layer for a Better Volatile Organic Compound Sensor Response

A. De Girolamo Del Mauro,[1] I. A. Grimaldi,[1,2] F. Loffredo,[1] E. Massera,[1] T. Polichetti,[1] F. Villani,[1] G. Di Francia[1]

[1]*Italian National Agency for New Technologies, Energy and Sustainable Economic Development (ENEA), Portici Research Center, Piazzale Enrico Fermi 1, 80055 Portici (Naples), Italy*
[2]*Department of Physics- University of Naples "Federico II", V. Cintia 1, 80126 Naples, Italy*

Received 28 April 2011; accepted 28 April 2011
DOI 10.1002/app.34777
Published online 11 August 2011 in Wiley Online Library (wileyonlinelibrary.com).

ABSTRACT: Volatile organic compound (VOC) chemical sensors increasingly rely on the use of polymer nanocomposites (PNCs) as sensing materials, thanks to the simple processability of polymers combined with the conductivity properties of nanoparticles dispersed in an insulating polymer matrix. Recently, inkjet printing (IJP), the main advantage of which is its patterning capability, was proven to be a reliable technique for the deposition of these materials. In this work, PNC chemical sensors were fabricated by IJP of a polystyrene/carbon black based ink. The sensor responses were measured upon exposure to acetone vapors and analyzed as function of the sensitive material geometry. Among the different realized geometries, the lines transverse to the interdigitated electrodes fingers resulted in the optimal configuration for the sensing layer in a VOC chemical sensor.
 J Appl Polym Sci 122: 3644–3650, 2011

Key words: nanocomposites; sensors; polystyrene

INTRODUCTION

Nanosized inorganic fillers dispersed in insulating polymeric matrices belong to the broader category of polymer nanocomposites (PNCs). The conductivity and mechanical stability properties of nanoparticles combined with the simple processability of polymers, low cost of production and of materials, possibility of easy and cheap manufacture of the large area devices, possibility of varying the composition, and hence, properties of the organic materials make the resultant hybrid system attractive in a wide range of polymer-based devices, such as light-emitting diodes,[1–3] photodiodes,[4] solar cells,[5] magnetic storage materials,[6] and gas sensors.[7]

The possibility of using polymeric nanocomposites for the manufacture of gas and vapor sensors relies on a fundamental phenomenon, which is related to the abrupt changes of the composite conductivity when the nanofiller concentration reaches the percolation threshold. When a polymer comes into contact with a specific substance, the absorption of the gas or vapor molecules changes its properties, that is, the polymer matrix volume (swelling). Correspondingly, a reduction of the filler volumetric fraction occurs, which determines a disrupt of the conductive paths and a change in electrophysical characteristics of the composites, which is reflected as a change of the electrical conductivity.[8–17]

Recently, inkjet printing (IJP) technology has rapidly emerged as a novel technique for the deposition of a wide variety of materials and has proven to be an useful technique in the deposition of PNCs films, which up to now, have prepared by techniques such as spin-coating or drop-casting.[18–21] The advantages of IJP over the aforementioned techniques are in its potential for printing on both nonflexible and flexible substrates, efficient use of materials, reduced waste products, low cost of the process, low processing temperature, and patterning capability. As for this last item, IJP technology assumes a key role in the feasibility of modifying the sensitive material geometry in a controlled and extremely easy manner to optimize the sensor response.

In this work, volatile organic compound (VOC) chemical sensors were fabricated by the printing of polystyrene (PS)/carbon black (CB) nanocomposites in different geometries realized with one or more lines differently orientated with respect to the transducer fingers. The sensor responses were measured upon exposure to acetone vapors and quantitatively analyzed. The device performances were compared in terms of sensitivity, response time, and limit of detection (LoD). Moreover, the sensing material morphology was characterized by means of scanning

Correspondence to: I. A. Grimaldi (angelica.grimaldi@enea.it).
Contract grant sponsor: Technologies and Research for the Application of Polymer in Electronic Devices (TRIPODE) project, financed by the Ministero dell'Università e della Ricerca; contract grant number: DM 20160.

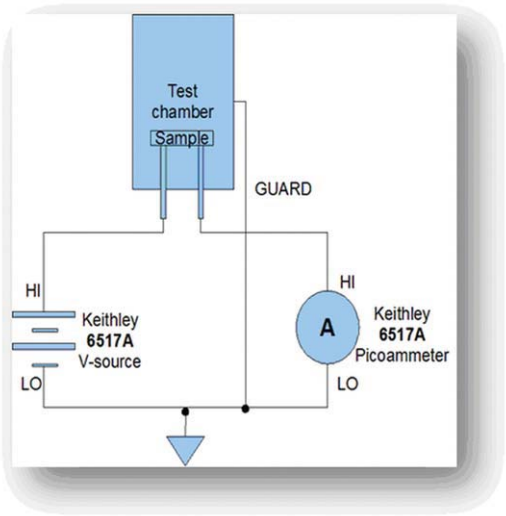

Figure 1 Electrical scheme for the resistance measurements. [Color figure can be viewed in the online issue, which is available at wileyonlinelibrary.com.]

electron microscopy (SEM) and atomic force microscopy (AFM) analysis.

EXPERIMENTAL

The employed substrates (5 × 5 mm^2) were made in alumina (Euroacciai s.r.l., Villa Carcina, Brescia, Italy), on which interdigitated Au electrodes were previously e-beam-evaporated and subjected to a lift-off photolithographic standard process. The interdigitated electrodes were characterized by the following geometrical parameters: the finger length was equal to 700 μm, the finger width was 100 μm, the gap distance between two adjacent fingers was 100 μm, and the number of fingers was 10.

The sensing material was a PS/CB composite. The atactic PS, supplied from Sigma-Aldrich (St. Louis, MO) (weight-average molecular weight = 25000), was chosen for its sensing properties to different organic chemical compounds (e.g., acetone, ethanol, toluene, benzene). The CB, used as conductive filler in the preparation of composites, was CB Pearls 2000 (Cabot Co.). This was a furnace CB material with a 1500 m^2/g specific surface area, a 12-nm average particle size, and a 150 g/L density. The PS matrix (80 mg) was dissolved in *N*-methyl-2-pyrrolidone, and the CB nanoparticles (20 mg) were dispersed in the polymeric solution (0.5 wt %) by means of an ultrasonic bath for 90 min. The PS/CB suspension was finally filtered with a 0.2-μm filter (polytetrafluoroethylene (PTFE)) with the aim of removing bigger agglomerates.

The processed dispersion was used as ink and printed onto a 50°C heated electrode/substrate system. The inkjet equipment was specially designed by Aurel s.p.a. (Modigliana, Italy) for the printing of inks onto flexible substrates as reels or single sheets and not flexible substrates. This printer used the piezoelectric drop-on-demand technology to eject droplets through a Microdropt Technologies GmbH (Nordersted, Germany) printhead (70-μm opening nozzle with a 180-pL droplet volume). The patterned sensing material geometries consisted of one or more lines created by overlapped droplet sequences (50% overlap, 0.5-Hz drop emission frequency, 0.05 mm/s printhead speed), differently oriented with respect to the transducer fingers.

The functional PS/CB ink was characterized by dynamic laser scattering (DLS) with an HPPS 3.1 instrument (Malvern Instruments, Malvern, Worcestershine, UK) to determine the particle size distribution of the filler in suspension and the dispersion stability in the solutions. The inks were characterized by DLS at different aging times.

Optical microscopy (Polyvar MET Reichert-Jung), SEM (LEO 1530), and AFM (Veeco, Dimension Digital Instruments Nanoscope IV, Plainview, NY) were used to investigate the morphology of the printed PS/CB layer. In detail, the AFM analysis was performed in tapping mode at ambient conditions.

A volt-amperometric technique, at a constant bias, was employed for sensor direct-current electrical characterization. The sensor response was measured upon exposure to acetone vapors at different concentrations (600, 1250, 2500, and 5000 ppm) in a test

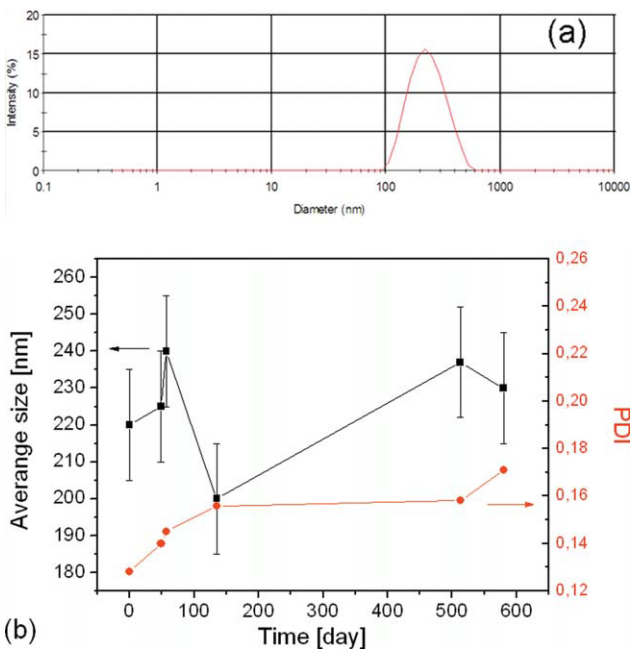

Figure 2 (a) Size distribution curve of the CB particles for the PS/CB dispersion. (b) (■) Nanoparticles average size and (●) PDI measured in the aging time from 0 to 600 days by DLS analysis. [Color figure can be viewed in the online issue, which is available at wileyonlinelibrary.com.]

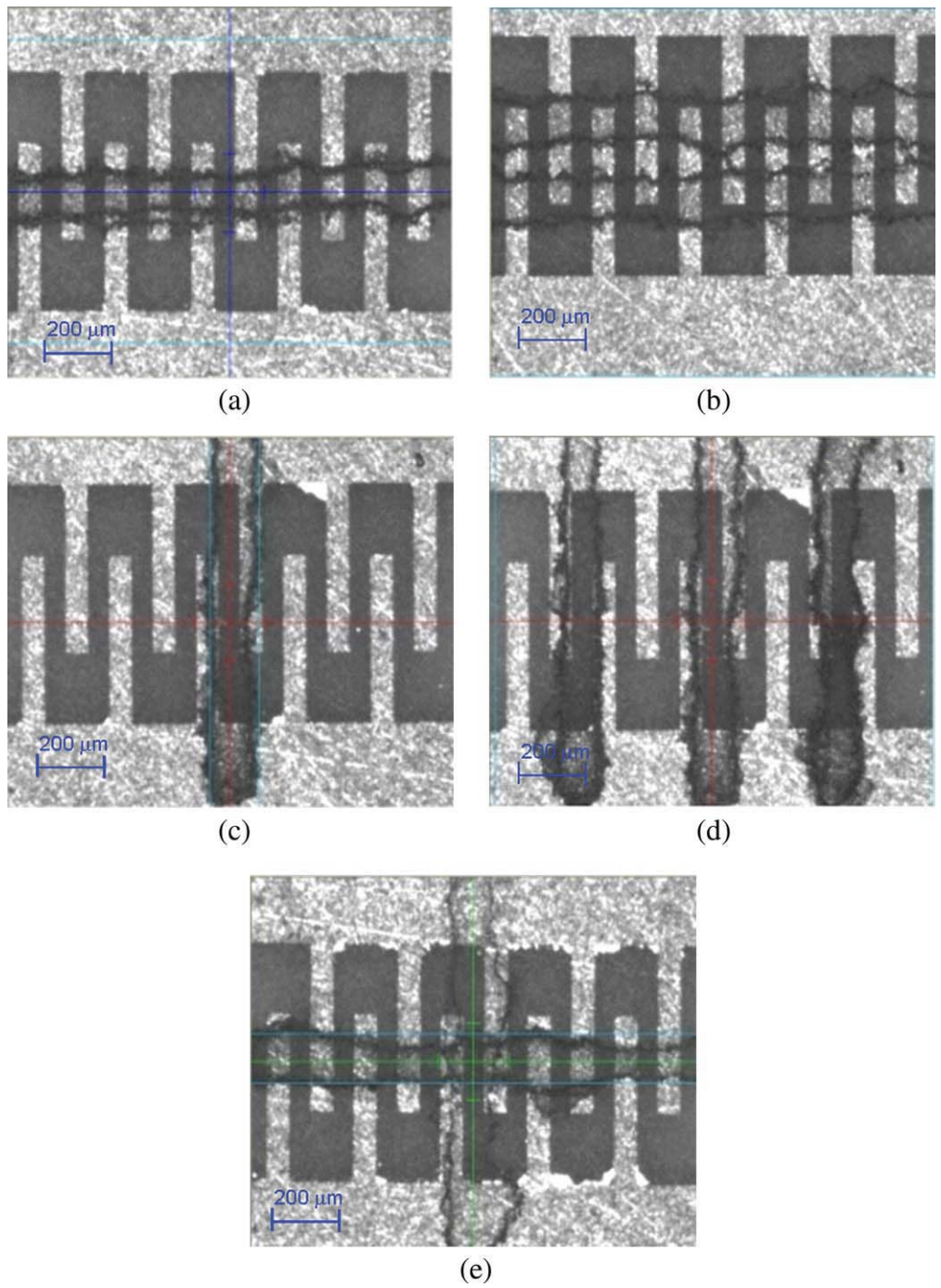

Figure 3 Optical micrographs of printed devices with different geometries: (a) single-line transverse, (b) double-line transverse, (c) single-line parallel, (d) three-line parallel, and (e) cross. [Color figure can be viewed in the online issue, which is available at wileyonlinelibrary.com.]

chamber that allowed us to monitor and control the pressure, flow rate, actual gas composition, humidity, and environmental temperature (600 ppm was the lowest gas concentration that could be introduced and kept constant). In this system (Kenosistec equipment), the device was placed in a stainless steel test chamber placed in a thermostatic box at a controlled temperature (20°C) and humidity (30%). The chamber was provided with an electrically grounded connector for bias and conductance measurements, as shown in Figure 1. A constant flow rate (500 cm^3/min) of the gas carrier, that is, nitrogen or synthetic air, crossed the test chamber. The carrier could be properly humidified through a water bubbler placed in a thermostatic bath. In this environment, characterized by a controlled temperature and humidity, the resistance value of the device in its equilibrium state was first measured (baseline); after that, an intentional disruption of the equilibrium state was produced by the introduction of a VOC

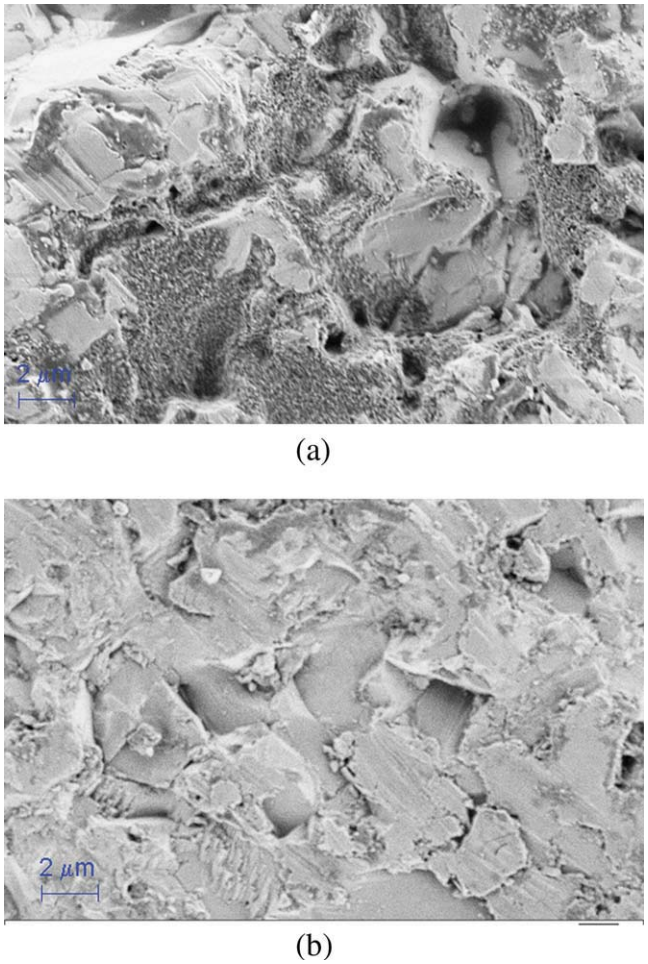

Figure 4 SEM images of (a) PS/CB printed on alumina substrate and (b) alumina. [Color figure can be viewed in the online issue, which is available at wileyonlinelibrary. com.]

analyte in a controlled amount and by its mixture with the gas carrier. To validate and monitor the gas mixture, a thermo Antaris IGS FTIR analyzer (Thermal Fisher Scientific, Waltham MA) was placed at the gas output to measure the chemical compound concentration in the test chamber with a resolution of parts per million. Hardware and software implemented on a work station allowed us to control and record the environmental parameters, device bias, and output signal; this made it possible for us to perform customizable automated tests on devices for the measurement of sensor parameters, such as sensitivity, response time, hysteresis, and LoD. In detail, the *sensitivity*, expressed in terms of the relative differential response and LoD, according to the conventional definition by IUPAC, is defined as the analyte concentration at which a sensor response corresponds to a signal-to-noise ratio equal to 3.

RESULTS AND DISCUSSION

Before deposition, the PS/CB dispersion was characterized by DLS analysis to investigate the average

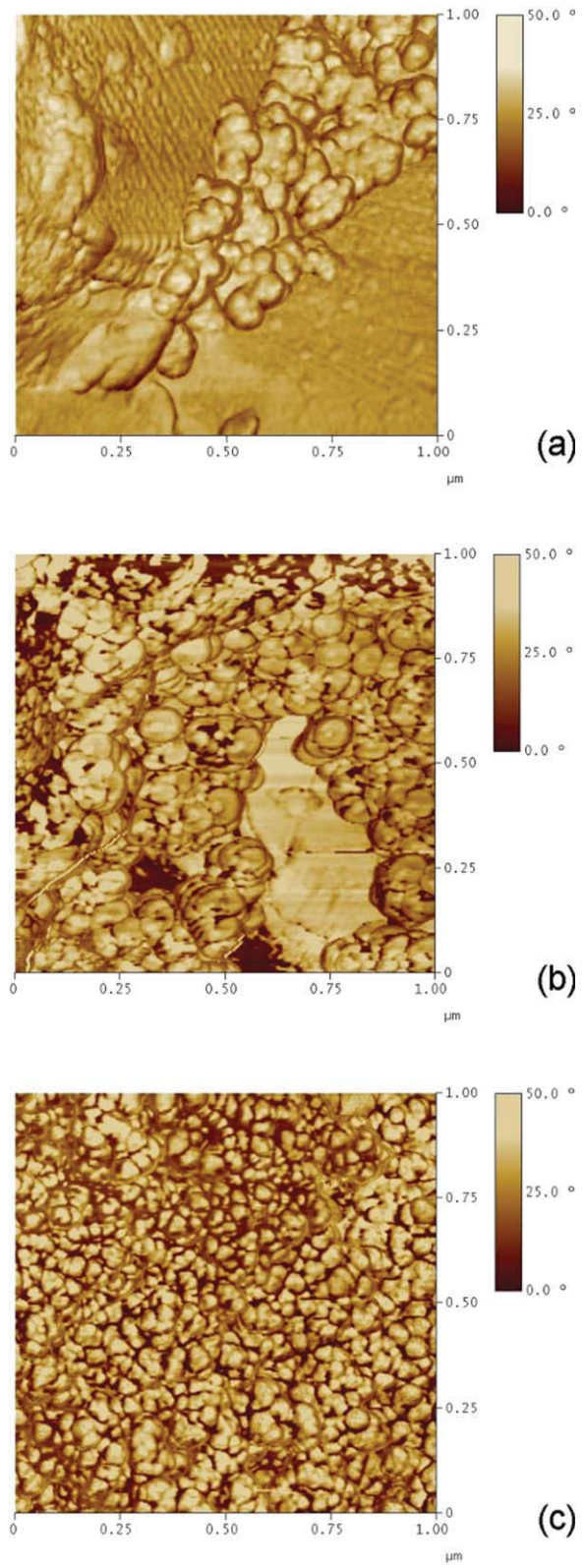

Figure 5 AFM phase images of the PS/CB samples printed in different zones of the substrate with (a) low, (b) partial, and (c) complete covering by the [Color figure can be viewed in the online issue, which is available at wileyonlinelibrary.com.]

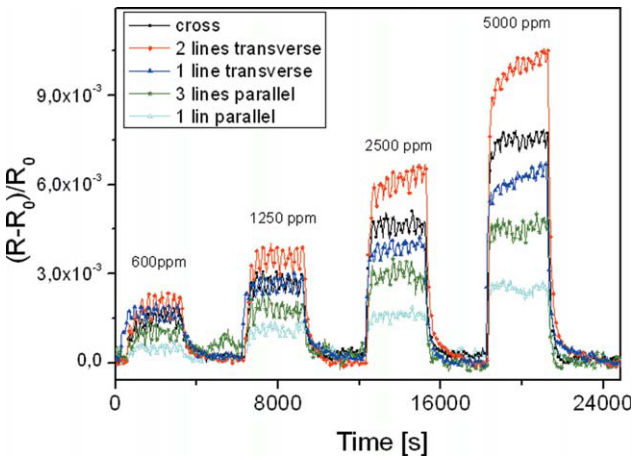

Figure 6 Three-layer sensor electrical responses to acetone vapors. [Color figure can be viewed in the online issue, which is available at wileyonlinelibrary.com.]

size distribution and the time stability. These measurements are reported in Figure 2. In particular, the distribution curve of the CB particle size in the dispersion presented a peak centered at 220 nm [Fig. 2(a)]. In addition, long monitoring of this dispersion showed a time stability of about 2 years, and the polydispersity index (PDI) values ranged between 0.12 and 0.18; this indicated that the dispersion was homogeneous [Fig. 2(b)]. The results of this analysis, combined with the viscosity (2.42 mPa s) and surface tension (46 mN/m) properties of the suspension, indicated that the dispersion could be employed as ink. Indeed, crucial elements of a dispersion for dispensing by an inkjet printhead are both the time stability and the particle size in suspension, which must be less than 1/100 of the nozzle diameter, to prevent clogging and blockage of the nozzle itself and the entire capillary. Therefore, these parameters indicated that the prepared PS/CB dispersion could be suitably processed by the IJP system.

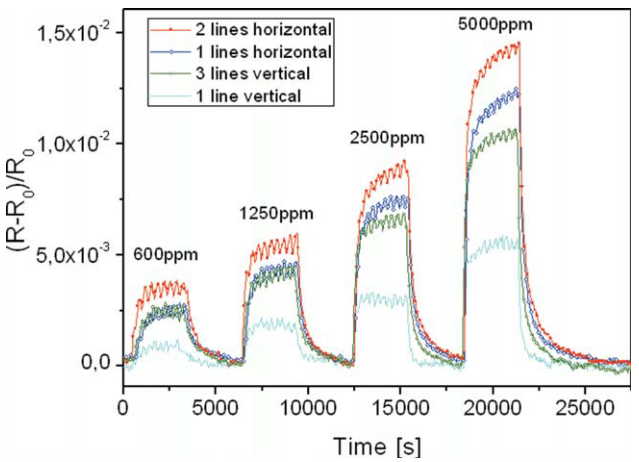

Figure 7 Five-layer sensor electrical responses to acetone vapors. [Color figure can be viewed in the online issue, which is available at wileyonlinelibrary.com.]

Successively, the devices were fabricated by IJP of the sensing material in five different geometries. Each geometry consisted of one or more lines parallel or transverse to the fingers of the interdigitated electrodes; the fifth geometry was a cross. Moreover, two different configurations were fabricated with three and five overlapped layers for each pattern with the aim of investigating the thickness effect on the sensor performances. The optical micrographs of the samples with different geometries are shown in Figure 3.

Before investigating the sensor device working conditions, we carried out the morphological analysis of the printed layers to get useful information on the sensor behavior. In Figure 4, the SEM image of a three-layer sample is shown as a comparison, with the simple substrate used as a reference. The printed PS/CB distribution on the substrate was clearly not uniform [Fig. 4(a)] because of just the substrate surface, which had a porous and sliver-shaped structure [Fig. 4(b)]. Thus, multiple layers of printed material were necessary to cover the pores and to obtain a continuous film. This morphological analysis was supported by the AFM investigations performed on the same samples. In particular, in Figure 5, the AFM phase images obtained by the scanning of 1×1 μm^2 surfaces of a three-layer sample in different zones are reported. The three images acquired at the printed line center were in agreement with the SEM analysis results concerning the nonuniformity of the deposited nanocomposite. Indeed, the printed material distributed differently on the substrate, as pointed out by pictures related to three typical configurations characterized by low [Fig. 5(a)], partial [Fig. 5(b)], and complete [Fig. 5(c)] coverage of the substrate by the nanocomposite.

However, if, on the one hand, the high roughness of the alumina substrate (average roughness $\approx$ 800 nm) and its sliver-shaped structure induced an ununiform distribution of the printed material, on the

TABLE I
Resistance, Sensitivity, LoD, and Response Time of the Three-Layer Sensors to Acetone Vapors

Morphology	Resistance (KΩ)	Sensitivity (S/ppm)	LoD (ppm)	Response time (s)
Cross	13.3	1.345×10^{-6}	100	100
Two-line transverse	38.5	1.837×10^{-6}	150	100
Single-line transverse	57.6	1.071×10^{-6}	180	100
Three-line parallel	95.7	0.8124×10^{-6}	560	100
Single-line parallel	1000	4.4394×10^{-7}	560	100

TABLE II
Resistance, Sensitivity, LoD, and Response Time of the Five-Layer Sensors to Acetone Vapors

Morphology	Resistance (KΩ)	Sensitivity (S/ppm)	LoD (ppm)	Response time (s)
Two-line transverse	8.6	2.4351×10^{-6}	60	>3000
Single-line transverse	8.9	2.188×10^{-6}	75	>3000
Three-line parallel	50	1.746×10^{-6}	200	>3000
Single-line parallel	175	1.056×10^{-6}	300	>3000

other hand, it ensured a better adhesion of the inkjet-printed ink.

After the sensing layer characterization, the electrical characterization of all of the manufactured sensors was performed. The electrical responses of the three-layer and five-layer devices to acetone vapors are shown in Figures 6 and 7, respectively. The device responses to the analyte were determined by the relative differential response, defined as $(R - R_0)/R_0$, where R is the sensor resistance upon its exposure to solvent vapors and R_0 is the sensor baseline resistance. The parameters that characterized the three-layer sensor performances are summarized in Table I, whereas the ones for the five-layer sensor are reported in Table II.

The results indicate that for whatever investigated geometry, the three-layer sensors were all faster than the five-layer devices. In detail, the *response time*, defined as the time required for the signal to change from 10 to 90%, for the three-layer devices was equal to 100 s; this was one order of magnitude lower than that of the five-layer devices (>3000 s). In this last case, the real time response value could not be estimated because the sensor response did not reach the saturation level in the investigated exposure time for each analyte concentration. This behavior could have been due to the different surface-to-volume ratios of the two configurations.

However, generally, the dynamic responses of sensors with different geometries are strongly influenced by R_0. In fact, when the different geometries of the three-layer configuration were compared (Fig. 6), the performances of the devices with transverse geometry were better than those of the parallel-geometry devices in terms of the sensitivity and LoD (see Table I). Both the increase of VOC sensitivity and the decrease of LoD meant an improvement of the performances corresponding to a lower base resistance of the devices.

This behavior could be easily explained through a comparison of the single-line geometries. Indeed, because the equivalent circuit of the transverse geometry was composed of multiple resistors placed in parallel, the device transduction effect in this geometry was enhanced with respect to the parallel geometry. The multiple-line geometries were ruled by the same mechanism, even if in a more complex manner.

The different geometries were realized with consideration of the minimum width dimension of the printed sensing material line and the transducer geometry (e.g., no more two transverse lines could be printed). In particular, the cross geometry was projected to increase the sensing surface with respect to the transverse single-line geometry. The dynamic response of the cross device effectively showed an improvement with respect to the transverse line in terms of both the sensitivity and LoD but in a less

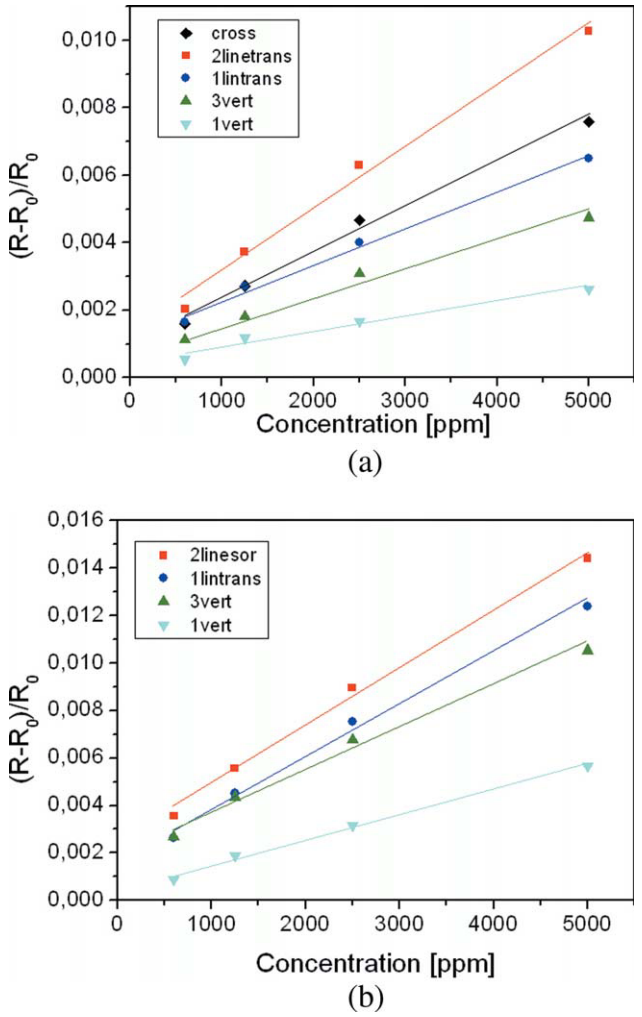

Figure 8 Calibration curves of the (a) three-layer and (b) five-layer sensors for all of the different geometries. [Color figure can be viewed in the online issue, which is available at wileyonlinelibrary.com.]

significant manner when compared with the transverse two-line geometry. This behavior was easily explained because the printed material along the parallel direction and not comprised between two contiguous fingers slightly influenced the electrical response (second-order effects). This statement was confirmed by the dynamic responses of the parallel geometries (single- and three-line geometries), which had the worst performances.

The correlation between the base resistance and sensitivity was also confirmed in the case of the five-layer devices (see Table II), which were characterized by a lower base resistance than the three-layer ones. Indeed, a higher number of multiple layers of sensing material increased the amount of the sensing material and induced the highest relative differential responses.

In Figure 8, the calibration curves of both configurations, three layer [Fig. 8(a)] and five layer [Fig. 8(b)], are reported. The data presented to compare all of the geometries were interpolated by linear fits. The calibration curve analysis allowed us to determine both the sensitivity (the angular coefficient of the calibration curve) and the LoD parameters. The results indicate that the electrical response varied linearly as the analyte concentration increased for all of the manufactured chemical sensors in the investigated concentration range (600, 1250, 2500, and 5000 ppm).

CONCLUSIONS

In this work, PNC-based chemical sensors were manufactured, and the relation between the device performances and the sensing material geometry was investigated. To this aim, IJP technology was employed to deposit the sensing material selectively and to take advantage of the patterning capability of this deposition method, and different geometries were realized in an extremely easy and controlled manner.

The results point out that the sensing material realized with a lower number of layers improved the device performances in terms of response time, thanks to a suitable surface-to-volume ratio. Moreover, the PNC-based chemical sensors fabricated by IJP of lines transverse to the fingers of the interdigitated electrodes showed the best sensitivity and LoD.

References

1. Madhava Rao, M. V.; Su, Y. K.; Huang, T.-S.; Tu, M.-L.; Wu, S.-S.; Huanga, C.-Y. J Electrochem Soc 2010, 157, H832.
2. Colvin, V. L.; Schlamp, M. C.; Alivisatos, A. P. Nature 1994, 370, 354.
3. Schlamp, M. C.; Peng, X.; Alivisatos, A. P. J Appl Phys 1997, 82, 5837.
4. Nyberg, T.; Zhang, F.; Inganas, O.; Curr Appl Phys 2002, 2, 27.
5. Liu, Z.; He, D.; Wang, Y.; Wu, H.; Wang, J. Solar Energy Mater Solar Cells 2010, 94, 1196.
6. Douadi-Masrouki, S.; Frka-Petesic, B.; Save, M.; Charleux, B.; Cabuil, V.; Sandre, O. Polymer 2010, 51, 4673.
7. Kim, Y. S. Sens Actuators B 2010, 147, 137.
8. Chatzandroulis, S.; Goustouridis, D.; Raptis, I. J Phys Conf Ser 2005, 10, 297.
9. Goustouridis, D.; Manoli, K.; Chatzandroulis, S.; Sanopoulou, M.; Raptis, I. Sens Actuators B 2005, 111, 549.
10. Convertino, A.; Leo, G.; Tamborra, M.; Sciancalepore, C.; Striccoli, M.; Curri, M. L.; Agostano, A. Sens Actuators B 2007, 126, 138.
11. Carrillo, A.; Martin-Dominguez, I. R.; Marquez-Lucero, A. Sens Actuators B 2006, 113, 477.
12. De Girolamo Del Mauro, A.; Grimaldi, I. A.; La Ferrara, V.; Massera, E.; Miglietta, M. L.; Polichetti, T.; Di Francia, G. J Sens 2009, to appear.
13. Shang, S.; Li, L.; Yang, X.; Wei, Y. Compos Sci Technol 2009, 69, 1156.
14. Lu, J.; Park, B. J.; Kumar, B.; Castro, M.; Choi, H. J.; Feller, J.-F. Nanotechnology 2010, 21, 255501.
15. Cakar, F.; Moroglu, M. R.; Cankurtaran, H.; Karaman, F. Sens Actuators B 2010, 145, 126.
16. Lonergan, M. C.; Severin, E. J.; Doleman, B. J.; Beaber, S. A.; Grubbs, R. H.; Lewis, N. S. Chem Mater 1996, 8, 2298.
17. Briglin, S. M.; Freund, M. S.; Tokumaru, P.; Lewis, N. S. Sens Actuators B 2002, 82, 54.
18. Ballarin, B.; Fraleoni-Morgera, A.; Frascaro, D.; Marazzita, S.; Piana, C.; Setti, L. Synth Met 2004, 146, 201.
19. Yoshioka, Y.; Jabbour, G. E. Synth Met 2006, 156, 779.
20. Loffredo, F.; Burrasca, G.; Quercia, L.; Della Sala, D. Macromol Symp 2007, 247, 357.
21. Loffredo, F.; De Girolamo Del Mauro, A.; Burrasca, G.; La Ferrara, V.; Quercia, L.; Massera, E.; Di Francia, G.; Della Sala, D. Sens Actuators B 2009, 143, 421.